

Ground test results of the electromagnetic interference for the x-ray microcalorimeter onboard XRISM

Miki Kurihara^{a,b,*}, Masahiro Tsujimoto^b, Megan E. Eckart^c, Caroline A. Kilbourne^d, Frederick T. Matsuda^b, Brian McLaughlin^d, Shugo Oguri^b, Frederick S. Porter^d, Yoh Takei^e, on behalf of of the XRISM *Resolve* team, Yoichi Kochibe^f

^aGraduate School of Science, The University of Tokyo, Bunkyo-ku, Tokyo, 113-0033 Japan

^bInstitute of Space and Astronautical Science, Japan Aerospace Exploration Agency, Chuo-ku, Sagami-hara, Kanagawa, 252-5210 Japan

^cLawrence Livermore National Laboratory, Livermore, CA 94550, USA

^dNational Aeronautics and Space Administration (NASA), Goddard Space Flight Center, Greenbelt, MD 20771, USA

^eInstitute of Space and Astronautical Science, JAXA, Tsukuba, Ibaraki 305-8505, Japan

^fFujitsu Limited, Saiwai-ku, Kawasaki, Kanagawa, 212-0014 Japan

Abstract. Electromagnetic interference (EMI) for low-temperature detectors is a serious concern in many missions. We investigate the EMI caused by the spacecraft components to the x-ray microcalorimeter of the *Resolve* instrument onboard the X-Ray Imaging and Spectroscopy Mission (XRISM), which is currently under development by an international collaboration and is planned to be launched in 2023. We focus on the EMI from (a) the low-frequency magnetic field generated by the magnetic torquers (MTQ) used for the spacecraft attitude control and (b) the radio-frequency (RF) electromagnetic field generated by the S and X band antennas used for communication between the spacecraft and the ground stations. We executed a series of ground tests both at the instrument and spacecraft levels using the flight-model hardware in 2021–2022 in a JAXA facility in Tsukuba. We also conducted electromagnetic simulations partially using the Fugaku high-performance computing facility. The MTQs were found to couple with the microcalorimeter, which we speculate through pick-ups of low-frequency magnetic field and further capacitive coupling. There is no evidence that the resultant energy resolution degradation is beyond the current allocation of noise budget. The RF communication system was found to leave no significant effect. We present the result of the tests and simulation in this article.

Keywords: low-temperature detector, x-ray microcalorimeter, electromagnetic interference, XRISM, high-performance computing.

*Miki Kurihara, kurihara@ac.jaxa.jp

1 Introduction

Electromagnetic interference (EMI) is a growing concern in modern astronomical instruments with increasing demands for high sensitivity and low noise. One of the areas of serious concern is the low-temperature detectors in space-borne or air-borne platforms. A noise level of $\mathcal{O}(10^{-18} \text{ W}/\sqrt{\text{Hz}})$ is required in a densely packed test bed consuming $\mathcal{O}(10^3 \text{ W})$. Examples can be found in Planck¹ high-frequency instrument² and SPIDER³ for cosmic microwave background observations and ASTRO-H⁴ soft x-ray spectrometer (SXS)^{5,6} for x-ray observations. More examples will follow in future missions.

*Resolve*⁷ x-ray microcalorimeter for the X-Ray Imaging and Spectroscopy Mission (XRISM)⁸ was designed to be almost the same as the SXS^{5,6} for ASTRO-H⁴ to recover its excellent science programs yet to be achieved due to the unexpected early loss of the mission by the malfunction of the spacecraft attitude control in March 2016. The SXS suffered from the EMI from the bus system that degraded the detector performance,⁹ which was only recognized after the integration

of the instrument into the spacecraft. Still, the SXS demonstrated its excellent performance beyond the requirement in the orbit.^{10,11}

Based on the lessons of the SXS, we started with an EMI verification program for *Resolve* and conducted a series of tests in 2021–2022 at JAXA’s Tsukuba space center both at the instrument and spacecraft levels. We recently finished the major part of these tests in August 2022. The purpose of this article is to report the results of the EMI ground tests and simulations so that it will be a reference in interpreting the in-orbit data with *Resolve* and in designing future instruments susceptible to EMI. Amongst various EMI effects, we focus on (i) the radiative EMI by the low-frequency magnetic field and (ii) the high-frequency electromagnetic field. The former was observed in the SXS,⁹ while the latter remains unverified in the SXS. The conductive EMI was also tested, which is described in a separate article.⁷

The article is structured as follows. In § 2, we give an overview of the *Resolve* instrument (§ 2.1) and the spacecraft (§ 2.2). The description is focused on the victims of the EMI, which are the microcalorimeter and anti-coincidence detectors and their signal chain (§ 2.1) and on the perpetrators of the EMI, which are the spacecraft attitude control and communication systems (§ 2.2). In § 3, we present the low-frequency magnetic field EMI results of the simulations (§ 3.1), instrument-level test (§ 3.2), spacecraft-level test (§ 3.3), and discuss the coupling mechanism (§ 3.4). In § 4, we present the high-frequency electromagnetic field EMI result in the same structure: simulation (§ 4.1), instrument-level test (§ 4.2), spacecraft-level test (§ 4.3), and discussion about the outcome (§ 4.4). The article is summarized in § 5.

2 *Resolve* onboard XRISM

2.1 *Resolve*

*Resolve*⁷ is one of the two science instruments onboard XRISM,⁸ which aims to achieve an energy resolution of 7 eV (FWHM) at 5.9 keV non-dispersively over a wide range of energy (0.3–12 keV). *Resolve* hosts an array of 6×6 x-ray microcalorimeter pixels thermally anchored to the 50 mK heat bath with a thermal time constant of 3.5 ms.¹² In each pixel, a HgTe absorber absorbs incoming x-ray photons and the resultant temperature rise is measured by a Si thermistor with a temperature-dependent impedance of $\sim 30\text{ M}\Omega$. Each microcalorimeter pixel is biased in series with a 140 M Ω load resistor, and the change in the voltage across the thermistor is the signal. Below the microcalorimeter array, an anti-coincidence detector¹² (anti-co) is placed for identifying particle events. The anti-co is a Si ionization detector biased in series with a 2.5 M Ω load resistor; the voltage across the load resistor is the signal, which is zero in quiescence. The bias voltage for the microcalorimeter pixels, but not the anti-co, is divided down by a factor of 121 between the connector at the dewar main shell and the top of load resistors¹³. The nine pixels within each quadrant of the array are connected to the same bias line. Each of these high impedance signal is converted into low impedance by a junction field effect transistor (JFET) source follower. The JFETs must be operated at 130 K, and, thus, are thermally isolated from the cold stage. Because of the commonalities and differences of the microcalorimeter and anti-co detectors, observation of the differential response is useful for evaluating potential coupling mechanisms of the noise.

The JFET signals are passed to the x-ray amplifier box (XBOX),⁵ which AC-couples, amplifies, and applies an anti-aliasing filter before digitizing them at 12.5 Hz sampling. The digitized signal is relayed to other room-temperature electronics called the pulse shape processor (PSP),¹⁴ which is responsible for x-ray event detection and reconstruction as well as collecting the detector

noise data. We use the spectra made from noise records of an 8k sample length (0.65536 s) for the frequency-domain data and dumps of continuous 50k samples (4.096 s) synchronous among all microcalorimeter and the anti-co channels for the time-domain data to evaluate the detector responses to EMI.

The detectors and JFETs are housed inside the dewar.^{15,16} A tank with superfluid He provides a stable thermal anchor of ~ 1.2 K. From there, two adiabatic demagnetization refrigerators (ADRs) work in series to cool the detector stage to 50 mK,¹⁷ controlled by room-temperature electronics called the ADR controller (ADRC).⁵ Between the detector stage and the dewar main shell are multiple isolated thermal shields made of Al of a few mm thickness. The dewar interior is cooled actively by five cryocoolers¹⁸ and passively by the He vapor cooling, and its exterior is passively cooled by radiative cooling toward deep space. In case of the depletion of superfluid He, a third ADR works to cool the He tank for an extended lifetime.^{19,20}

The dewar is an Al vacuum vessel, leak-tight on the ground under air, thus constituting a Faraday cage against the external EMI environment. For x-ray observations in orbit, the dewar needs to be open along the x-ray light path. An apparatus called the gate valve (GV) is installed at the top of the dewar, which is kept closed on the ground and during launch. The GV will be permanently opened using a non-explosive actuator during the commissioning phase after the spacecraft out-gassing settles. The GV door has a Be window of ~ 270 μm thickness²¹ to transmit x-rays above ~ 2 keV.

2.2 Spacecraft

XRISM is planned to be launched in 2023 from the JAXA's Tanegashima space center into a near-Earth orbit with an altitude of 575 km and an inclination of 31 degrees. The spacecraft is in the final integration testing, as of writing, since April 2022 at the JAXA's Tsukuba space center. The structure of the spacecraft inherits the design of ASTRO-H (Figure 1). It has a weight of 2.3×10^3 kg and an envelope size of 7.9, 9.2, and 3.1 m respectively for the height (z), length (x), and width (y). The main body is composed of eight side panels (SP1–8) of 990×3100 mm^2 in size, whose inside has the top, middle, and lower plates perpendicular to the SPs standing on the bottom structure. For *Resolve*, the x-ray mirror is placed on the top panel, the dewar is upright on the bottom structure, and room-temperature electronics are inside the body on the SPs. The solar array panels are stored in SP2 and SP4 at launch and are deployed in parallel with SP3, which are oriented toward the Sun. A part of SP7 is a lattice window exposed to deep space to cool the dewar surface radiatively.

For the attitude control of the spacecraft, the reaction wheels (RWs) and the magnetic torquers (MTQs) are used as main actuators. The RWs are composed of four units with the base momentum of a 3000 rpm rotation, which are used to rebalance the angular momentum within the spacecraft for pointed observations and maneuvering. The MTQs dump the accumulated angular momentum against the Earth magnetic field. Three MTQs are installed inside SP3 for the x axis and SP5 for the y and z axes. Each MTQ is a solenoid of a 920 mm length and a 34 mm radius, which generates the maximum magnetic moment of 900 A m^2 for a ± 35 V bipolar DC drive. The field strength is controlled by changing the duty ratio of the DC with pulse width modulation (PWM) at 127 Hz frequency. This is close to the thermal time constant of the detector, and can cause significant degradation when coupled. This was indeed observed in the SXS,⁹ but its coupling path (magnetic or conductive) has not been clarified.

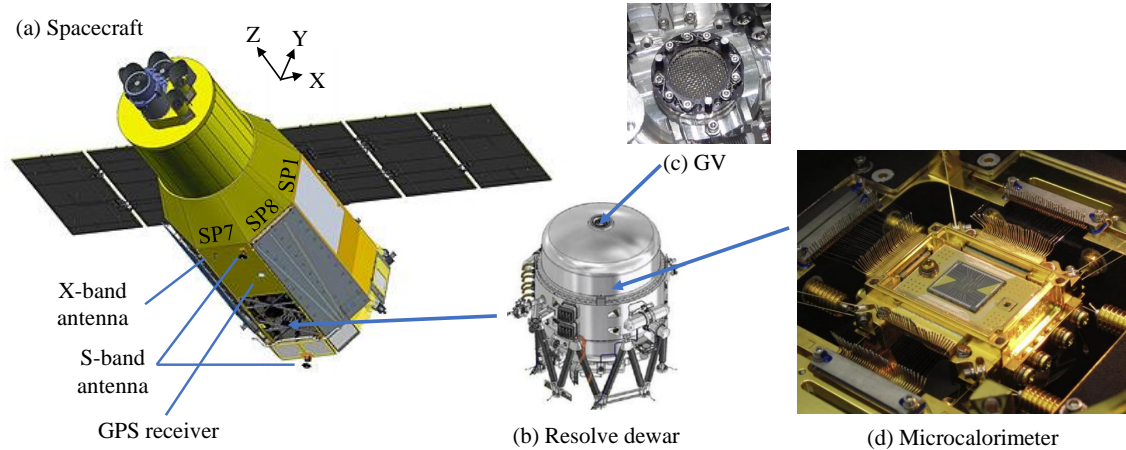


Fig 1: Illustration of the spacecraft and the *Resolve* instrument. (Photo (c) is from Ishisaki et al.⁷)

For communication with the ground, the spacecraft has four S-band and two X-band antennas. A half of them (two S-band and one X-band antennas) are located outside of SP7, while the other half are outside of SP3. The S-band is used both for uplink and downlink at 2 GHz, while the X-band is used only for downlink at 8 GHz. All of them use a cross-dipole antenna with a reflector to increase the forward-to-backward ratio. Another use of radio frequency (RF) is the GPS receivers outside of SP3 and 7. The electronics for the RF modulation/demodulation, filtering, and amplifying are installed inside of the SPs. These RF equipments, in particular those for downlink with strong emission local to the spacecraft, are the sources of high-frequency electromagnetic field. Because the *Resolve* dewar constitutes a Faraday cage with the GV closed on the ground and early in the orbit, the RF signals would not affect the detector inside the dewar. This was indeed the case for the SXS, which ended its life before the GV was opened in the orbit. However, when the GV will be opened for *Resolve*, the cage is broken with a ~ 35 mm diameter hole left open and we may expect RF interference with a frequency higher than its cut-off at ~ 2 GHz. A particular concern is the RF emission from the X-band or S-band antenna outside of SP7, which can diffract into the spacecraft main body through the opening in SP7 and reach the detector through the opened GV. The modulation in the carrier frequency used for communication may load energy to the detector that varies in time within its bandpass. This could not be verified for the SXS and thus must be investigated for *Resolve*.

3 Magnetic EMI

3.1 Simulation

We start with the simulation of the magnetic field generated by the three MTQs. The MTQ has a large inductance (6.7 H) with a cut-off frequency of 0.68 Hz, which is much smaller than its PWM drive frequency. The magnetic field is approximated as DC, thus we calculated the static solution of Maxwell's equations. The AC component can be calculated by scaling the DC simulation results in the post-processing. We used the Maxwell software¹ provided by ANSYS based on the finite element method (FEM) solver. A model was made by simplifying the spacecraft main body and the *Resolve* dewar (figure 2 a). A personal computer is sufficient for this simulation.

¹See <https://www.ansys.com/products/electronics/ansys-maxwell> for detail.

The results are shown in Figure 3 for the three MTQs separately, which generates the magnetic field of different strengths of $\mathcal{O}(10 \mu\text{T})$ and orientations around the dewar. A conceivable part to pick up the magnetic field is the harness from the room-temperature electronics (XBOX and ADRC) that goes into the cold stages inside the dewar. The cross-section of the dewar including their feed-through is chosen for visualizing the calculated field.

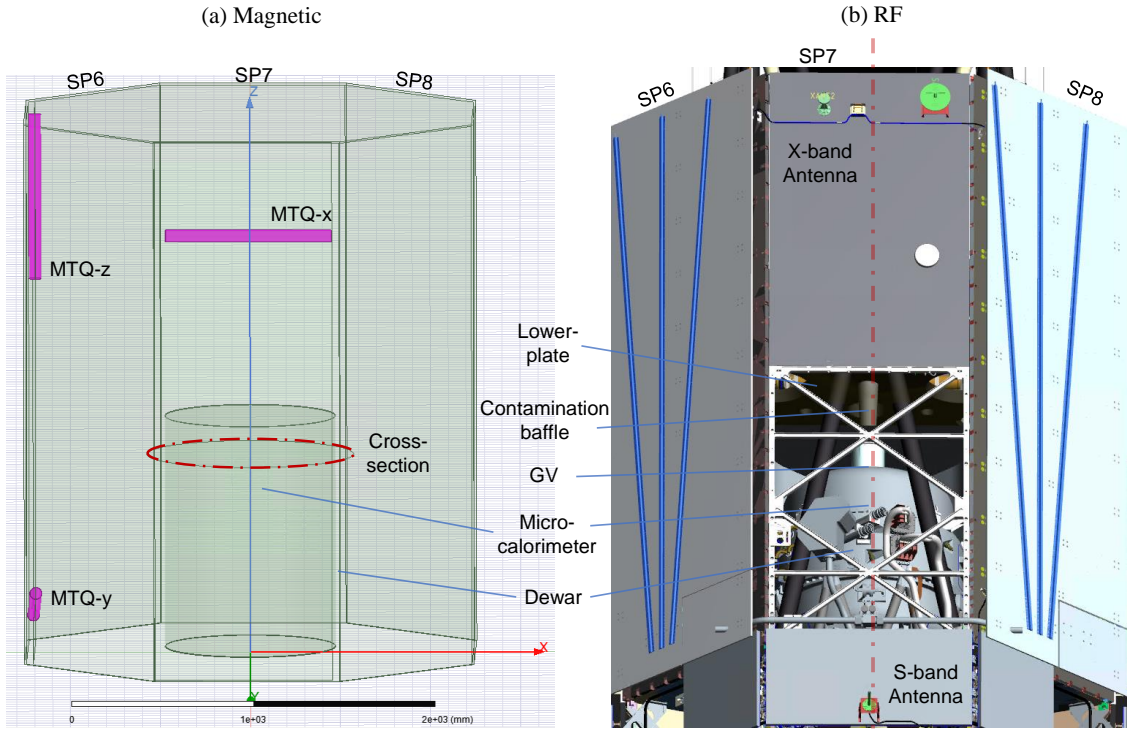


Fig 2: Simulation models of (a) magnetic and (b) RF EMI seen from the SP7 in a slightly upward direction. The emission sources (a; three MTQs and b; two RF antennas) and the evaluation plane of the simulation (a; circular cross section perpendicular to the z axis including the feed-through and b; cross section perpendicular to the x axis including the detector center) are shown in red dashed-and-dotted curve or line.

3.2 Instrument-level test

We performed the magnetic EMI test during the instrument-level test using the flight-model hardware of *Resolve* on September 14–15, 2021. The test was designed to measure the detector response against the magnetic field injection. Despite the nearly DC behavior of the magnetic field, its AC component is more important in the microcalorimeter bandpass. We need to simulate the PWM shape precisely in the time domain. We thus used the engineering model (EM) unit of MTQ left from ASTRO-H, which is the same design as the ones used for XRISM, and drove it in the same way as the flight MTQ driver does.

Figure 4 shows the setup of the instrument-level test for the magnetic EMI. The EM MTQ was placed at a flight position of the MTQ- y relative to the dewar (Figure 4 a). The PWM shape was made with a function generator, which was amplified by a bipolar power supply (Figure 4 c). The magnetic field was measured using magnetometers sensitive to the AC field up to 500 Hz

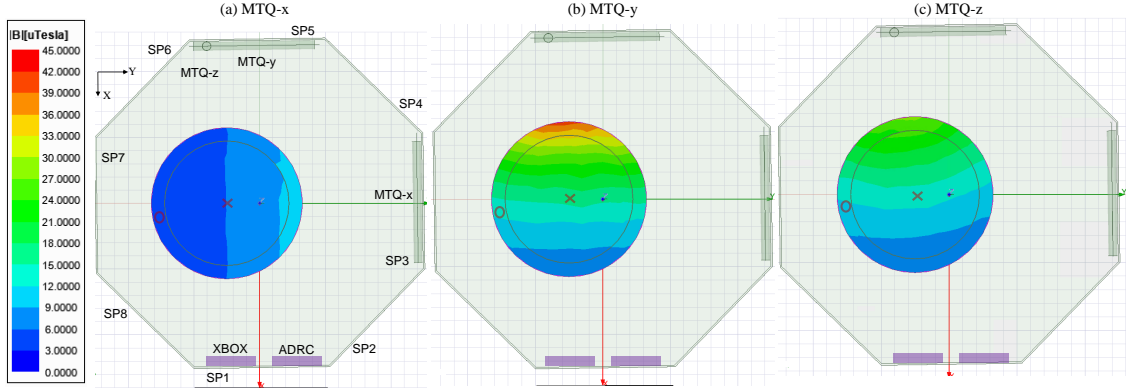


Fig 3: Results of the magnetic simulation. The magnetic field strength $|B|$ is given in the unit of μT on the plane perpendicular to the z axis at the height of the feed-through of the dewar harness leading to the ADRC/XBOX (Figure 2 a). The position of the detector and the feed-through is shown with the cross and the circle, respectively.

for the three axes (Figure 4 a). Unlike the spacecraft-level test, we have several flexibilities to investigate the coupling nature and possible mitigation: (1) we can change the relative distance between the MTQ and the dewar arbitrarily to examine the contribution of the magnetic coupling, and (2) we can test wrapping the harness between the room-temperature electronics and the dewar with a magnetic shield material.

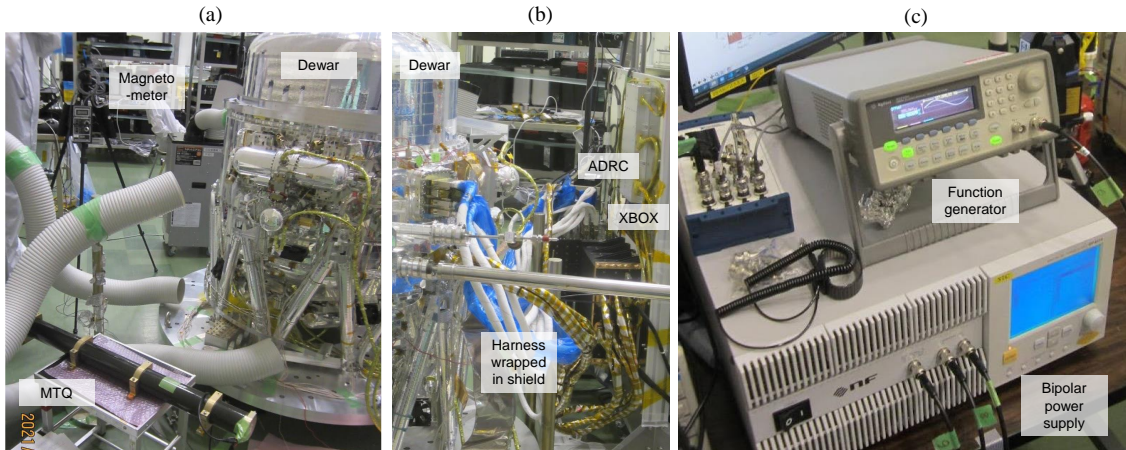


Fig 4: Setup for the magnetic EMI instrument-level test: (a) SP5 and (b) SP8 side of the dewar (Figure 3), and (c) drive electronics.

We had three configurations for the distance between the dewar center and EM MTQ: the flight value (1135 mm) and 1.56 and 2.12 times of it. In each configuration, the MTQ was driven in various duty ratios (20, 30, -70, and 80%). Here, -70% duty denotes 70% duty with the negative polarity (-35 V). The microcalorimeter bias setting was also changed from nominal (1.6 V) to zero or a high (5.0 V) value. A part of this test was repeated after wrapping the harness with the cobalt-based magnetic shield (2705M) provided by Metglas[®], Inc²(Figure 4 b).

²See <https://metglas.com/wp-content/uploads/2016/12/2705M-Technical-Bulletin.pdf> for detail.

Figure 5 shows the detector response in the frequency domain using the 8k noise spectra with and without the MTQ with different detector biases. A strong signature of the MTQ PWM frequency (127 Hz) and its harmonics was observed on both calorimeter and anti-co channels when the MTQ was operated. For the anti-co, the magnitude of the interference was independent of bias, whereas for the microcalorimeter channels, the interference was stronger at zero bias than at nominal bias. Figure 5 shows the detector response in the time domain folded by the PWM frequency using the bipolar power supply monitor reading for the input voltage (red) and the microcalorimeter output for two selected pixels (blue and orange) as well as anti-co's (green). The time between the input and output data set is shifted to match the PWM edges to the microcalorimeter peaks and valleys as their relative time was not calibrated. Figure 5 shows the strength of the microcalorimeter noise power at 127 Hz for all pixels in the array. The distribution is characterized by the enhanced response in the pixels of a multiple of 9 (0, 9, 18, and 27) and an elevated level in the upper half of the array than the lower half. These remarkable features were consistently observed throughout the test. The measurement with the magnetic shield wrapping the harness did not show significant difference beyond the systematics.

3.3 Spacecraft-level test

We performed the magnetic EMI test during the spacecraft-level test on June 9, 2022. We operated the three units of the MTQs separately for the ± 90 and $\pm 45\%$ duty ratio and collected the detector noise spectra (a) to confirm the result obtained in the instrument-level test (§ 3.2) and (b) to characterize the transfer function from each unit of the MTQ to the microcalorimeter. We also operated the three MTQs with the PWM duty ratio of $(x, y, z) = (\pm 30, \mp 30, \pm 30)\%$ for an overnight integration with x-rays and compared the result with another overnight result without the MTQ to assess the degradation of the energy resolution by the presence of the strong 127 Hz and its harmonic lines in the noise spectra (Figure 5). The duty ratio was chosen to be the same among the three axes so that the time-domain peaks (Figure 5) match for the worst case; the opposite polarity for y is to negate the opposite polarity of the MTQ- y driver by design.

Figure 6 shows the microcalorimeter noise power at $127n$ Hz ($n = 1, 2, 3$) against the MTQ operation for each unit. The response was the strongest in the order of y, z , and x . No significant difference was found between the opposite polarities. Figure 6 shows the noise power at 127 Hz as a function of the PWM duty ratio both in the instrument- and the spacecraft-level tests.

The MTQ duty ratio keeps changing in the orbit. We simulated its behavior, along with the RW, during the spacecraft thermal-vacuum test in August 28–29, 2022 to assess their impact in practice. The energy resolution of the microcalorimeter averaged over a four-hour period with the MTQ and RW operation and another period without the MTQ and RW operation was compared using calibration x-ray sources. No significant difference was found and the risk of science impact is low. In case the increased coupling for some reasons in the future, we have a backup option ready to notch the 127 and 254 Hz lines in the onboard signal processing.

3.4 Discussion

Based on the results obtained in the instrument-level (§ 3.2) and spacecraft-level (§ 3.3) tests and the simulation (§ 3.1), we speculate how the MTQ couples with the microcalorimeter detector. We note that the features observed in the *Resolve* ground tests were very similar to those identified during SXS spacecraft-level tests, including the enhanced interference in specific pixels, the MTQ

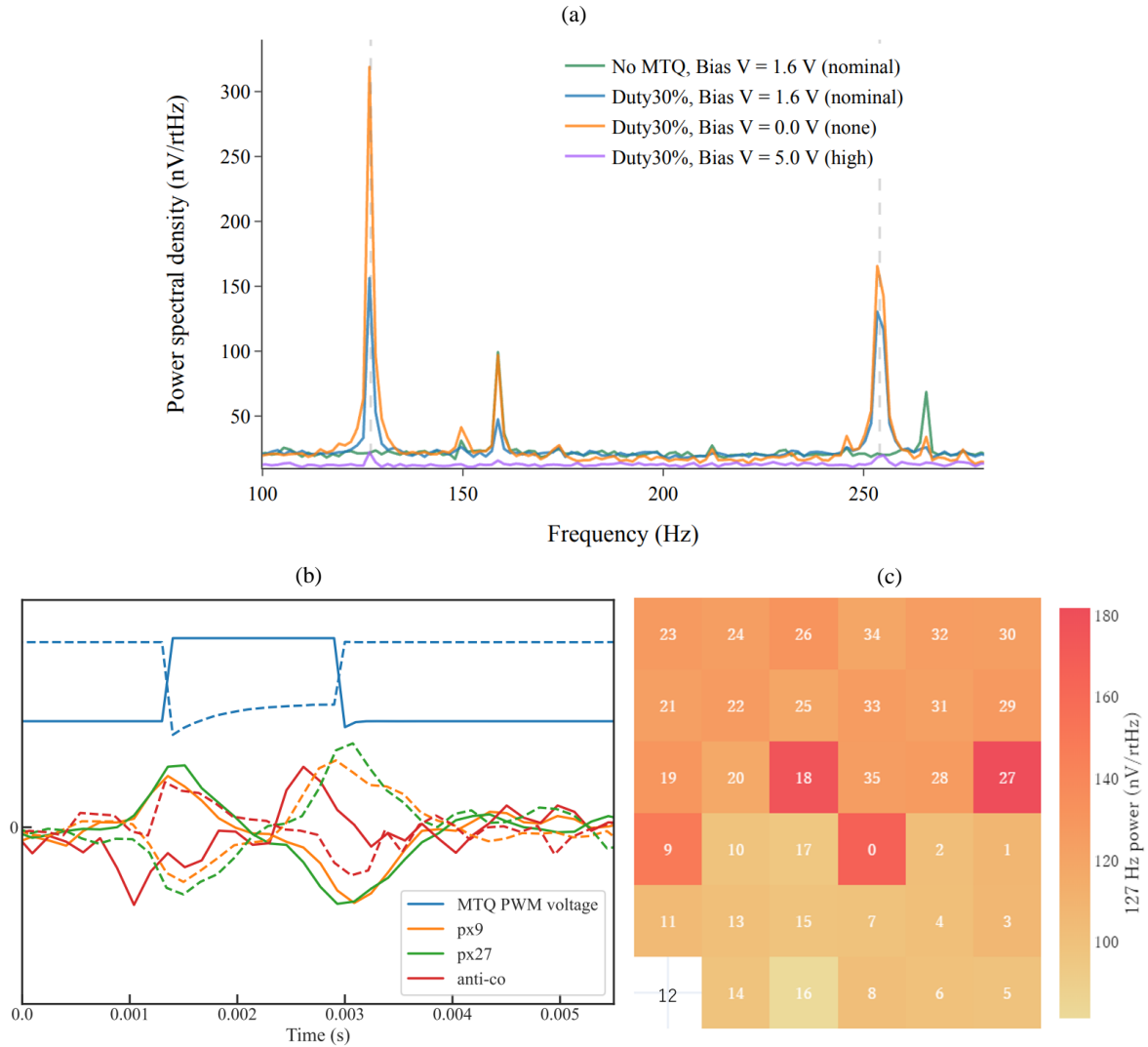


Fig 5: Results of the magnetic EMI instrument-level test: (a) Frequency-domain data of pixel 9 with varying detector bias (blue for nominal, violet for high, and orange for none) with a 30% PWM duty of the MTQ. The PWM frequency (127 Hz) and its second harmonics are shown with dashed lines. Data of nominal bias without MTQ operation (green) is shown for comparison. The 150 and 156 Hz lines are, respectively, the third harmonic of the commercial AC and a cryocooler drive.^{22,23} (b) Time-domain data of the drive voltage (blue) and response of the microcalorimeter for pixel 9 (orange), 27 (green), and the anti-co (red) during the 20% (solid) and 80% (dashed) duty drive. The anti-co signal is intrinsically opposite in polarity and shifted slightly in phase from that of the microcalorimeter. (c) Pixel dependence of the noise power at 127 Hz when the MTQ was operated with a 30% PWM duty using the 8k noise spectra. Pixel 12 yielded no noise spectra by being interrupted by constant x-ray illumination by the ⁵⁵Fe calibration source.

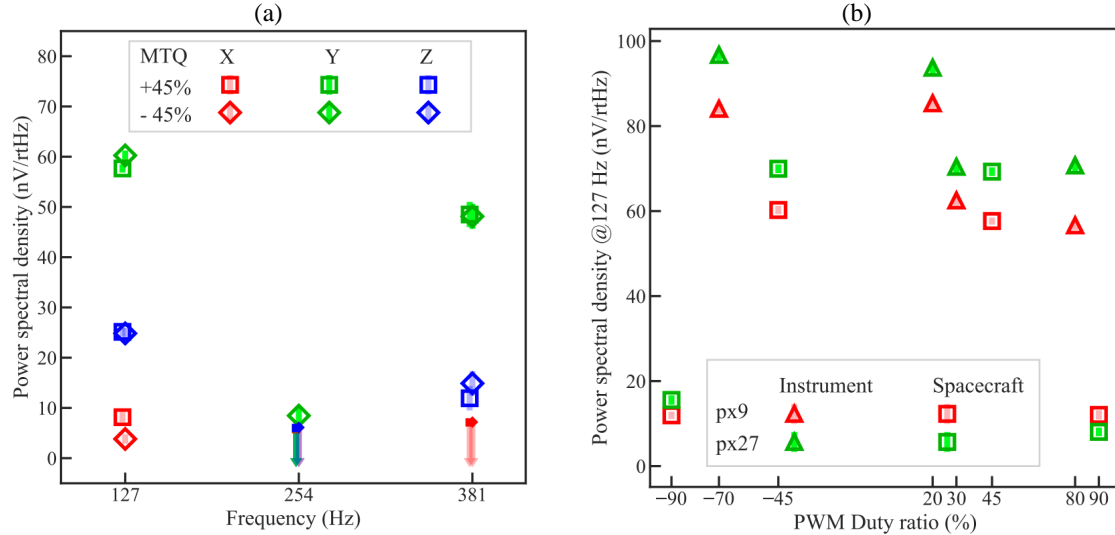


Fig 6: Results of the magnetic EMI spacecraft-level test: (a) Line power of px 9 at $127n$ Hz ($n = 1, 2, 3$) for the three MTQ units operated at $\pm 45\%$ duty ratio. The underlying continuum was subtracted. The error bars are estimated from the continuum levels of the frequency neighbors. The upper limit of 3σ is given in case of no detection. (b) Line power at 127 Hz for different duty ratio in the instrument- and spacecraft-level tests.

axis- and polarity-dependence of the detector response, the nature of the scaling with MTQ duty cycle, and the level of energy resolution degradation. The consistency between *Resolve* and SXS test results lends support to the identification of the likely MTQ coupling mechanism outlined below.

First, the coupling is likely via the magnetic field. This is illustrated by the distance dependence between the MTQ and the dewar in the instrument-level test (Figure 7). The dependence of the 127 Hz power in the detector noise spectra decreases as the distance increases. Because other coupling mechanisms, such as conductive coupling from the MTQ driver to the *Resolve* room-temperature electronics or low-frequency RF coupling from the MTQ driver, are not expected to exhibit such dependence, we argue that the magnetic coupling is dominant. Indeed, the observed distance dependence is quite similar to the simulated dependence of the field strength $|B|$ at the dewar center (Figure 7). This explains why we observed the strong axis dependence of the MTQs (y , z , and x in the decreasing order) in the spacecraft-level test (Figure 6). It is mostly attributable to the distance between each MTQ unit and the dewar (Figure 7).

The magnetic coupling is also supported by the MTQ polarity dependence of the response. The magnitude of response is the same between the two polarities (Figure 6) and the sign of the response is the opposite for opposite polarity in the time domain (Figure 5). Such behavior excludes the possibility that the response is a function of the input power expected in conductive or RF coupling.

We speculate that a particular part of the instrument is sensitive to a particular direction of the magnetic field. We injected local magnetic field using a portable solenoid driven with a 127 Hz sine wave and found that the harness between the room-temperature electronics (ADRC, XBOX) and the dewar and their ends are particularly sensitive. There might be other susceptible places, in particular inside the dewar, which was not accessible with the portable solenoid.

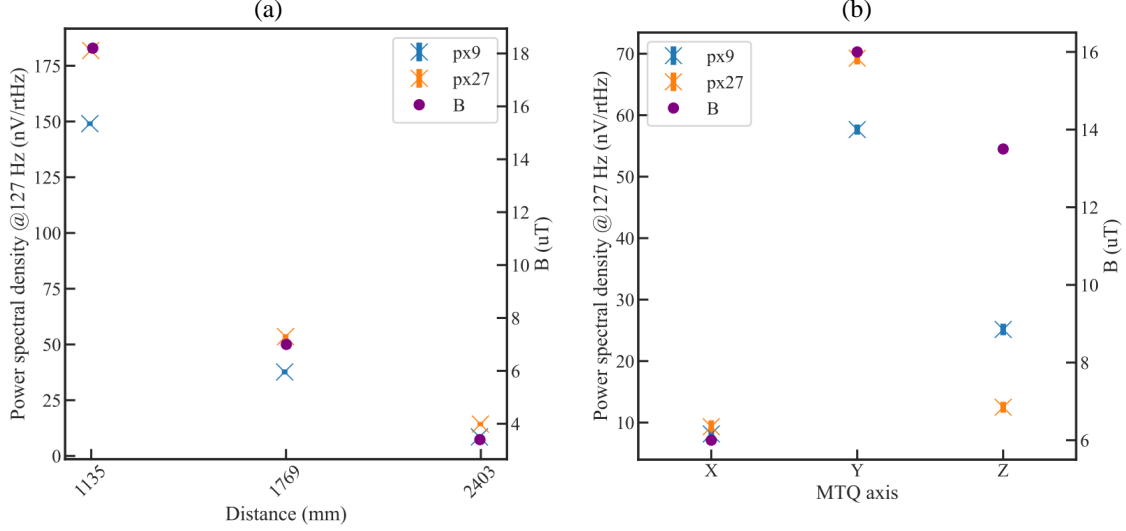


Fig 7: Comparison of the measurement and simulation: (a) Distance dependence of the 127 Hz power (pixels 9 and 27) and the simulated magnetic field strength $|B|$ at the dewar center in the instrument-level test (§ 3.2) with the EM MTQ driven at a 30% duty. (b) Axis dependence of the 127 Hz power (pixels 9 and 27) and the simulated magnetic field strength $|B|$ at the dewar center in the spacecraft-level test (§ 3.3) with the flight MTQs driven at a 45% duty.

If the nearly DC magnetic field is the path for the coupling, why do we observe an AC response in the microcalorimeter? This can be studied by using the time-domain data in Figure 5. The spacing between rising and falling edges of the input voltage $V_{\text{input}}(t)$ coincides with that between the peak and the valley of the microcalorimeter output in all tested duty cycles. The magnetic field is smoothed in time for its large inductance with $B(t) \propto \int V_{\text{input}}(t)dt$, but the induced voltage is $V_{\text{ind}}(t) \propto dB(t)/dt \propto V_{\text{input}}(t)$. If this further couples capacitively, the noise voltage would be $V_{\text{noise}}(t) \propto dV_{\text{ind}}(t)/dt \propto dV_{\text{input}}(t)/dt$. This explains the edge–peak relation in the time-domain data. The microcalorimeter response is smaller for the 90% duty than the 45% duty in the spacecraft-level test (Figure 6). This is probably because the rising and falling edges are close in time for the 90% duty so they cancel to some extent when arithmetically added.

The likely place of the capacitive coupling can be investigated using the pixel dependence in Figure 5. The pixels with a multiple of 9 (pixels 0, 9, 18, and 27) are particularly susceptible to the magnetic EMI. This is related to the readout wire layout from the microcalorimeter.¹³ Figure 1 (d) shows the close-up view, in which two bundles of wires (18 pairs of signal and return for each pixel) come out of the detector array. One bundle reads the upper half of the array and the other the lower half. This part with a high impedance before the JFET impedance conversion is particularly sensitive to external radiative noise, hence a likely site of the capacitive coupling. The signal and return wires are aligned alternately, and all signal wires but the outermost (pixels 0, 9, 18, 27) are in between grounded return wires. This could explain the peculiar pixel dependence of magnetic coupling.

We have ample evidence that the magnetic interference is not acting through heating, but is purely electrical. The first indication is that the pickup is seen on the anti-co (Figure 5), which is a non-thermal device. Furthermore, the signal in the time domain is bipolar (Figure 5). Finally, the detector bias dependence (Figure 5) is not consistent with heating. With no bias, the microcalorimeter would not work as a thermal detector. Still, the strong MTQ noise lines were

observed, illustrating the electrical nature of the input. This is in contrast to the thermal nature of the input found in the low-frequency noise by the cryocooler micro-vibration interference of the *Resolve* instrument.^{22,23} In fact, the dependence of the magnetic coupling on bias for a particular pixel appears to scale with the expected temperature- and frequency-dependent impedance of the thermistor.

4 RF EMI

4.1 Simulation

For RF EMI, we also start with the simulation, which requires massive computational resources unlike the low-frequency magnetic EMI (§ 3.1). RF simulation is typically performed with a mesh size $\sim 1/20$ of the wavelength (i.e., 2 mm for the X-band) with a model detailed to the scale. This is far smaller than the spacecraft size. Therefore, in spacecraft RF simulations, simplified models with hybrid solvers are often used. In this study, however, we use the detailed CAD model with a single solver for simulating the entire spacecraft.

For the solver, we use the finite difference time domain (FDTD) method.²⁴ This solves a discretized Maxwell's equations on the Yee's lattice.²⁵ We adopt the `Poynting` for Microwave software³ by Fujitsu. For the computer, we use Fugaku,²⁶ a high-performance computing facility in RIKEN, which is also manufactured by Fujitsu. The most detailed CAD model for the entire ASTRO-H spacecraft was used with some modifications in accordance with the design changes for the XRISM. The materials are replaced with the perfect electric conductor. The perfect matched layer was set as the boundary condition for the simulation box (Figure 2 b).

We injected the maximum operational power used for transmission (31.6/36.3 dBm respectively for the S/X-band antenna outside of SP7; the closer to the dewar of the two for the S-band antenna). The simulation was run for 25/23 μs in time and a total mesh of 1.9×10^{11} in space using 1024 nodes of Fugaku for 3 hours. A snapshot at 11.1/10.2 ns is shown in Figure 8. The calculated field strength at the interface above the GV is $1.5 \times 10^{-4}/5.6 \times 10^{-3} \text{ V m}^{-1}$, which corresponds to $-106/-63$ dBm, respectively for the S/X-band.

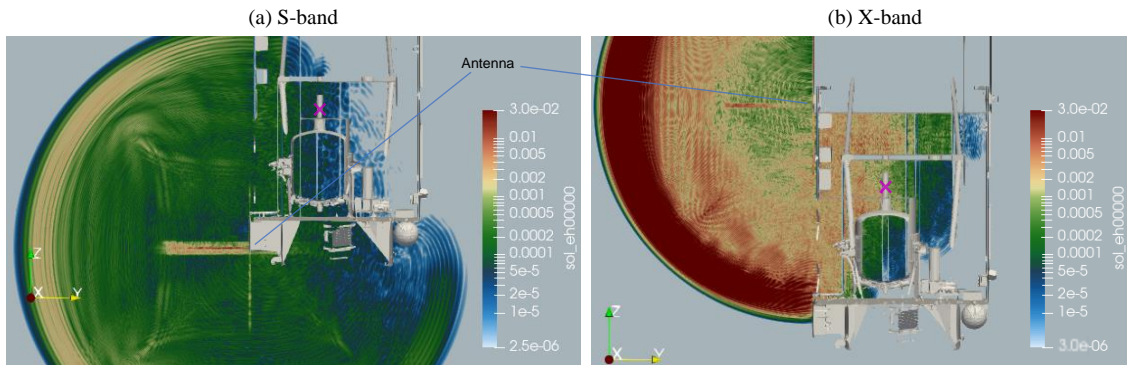


Fig 8: Results of the RF simulation for the (a) S-band and (b) X-band antenna on SP7. The field strength $|\mathbf{E}|$ is given in the unit of V m^{-1} on the plane vertical to the x -axis including the detector (Figure 2 b). The interface is marked with the magenta cross. The horizontal structure from the antennas is an artifact of the simulation. Paraview²⁷ is used for visualization.

³See <https://www.fujitsu.com/jp/solutions/business-technology/tc/sol/poynting/> for detail.

4.2 Instrument-level test

We performed the RF EMI test during the instrument-level test using the flight-model hardware on February 24 and 28, 2022. The test was designed to measure the detector response against the RF injection at the S and X-band from above the dewar by opening the GV. Figure 9 shows the experimental setup. We avoided moving the entire instrument to an EMC test room in a different building to avoid various risks, thus the test was performed in a clean room continued from other tests. Special apparatuses described below for this test are not mechanically compatible with the spacecraft structure, so the instrument-level is the highest level of integration to perform this test.

In the setup, we need to meet two requirements: one is to keep the dewar vacuum and the other is to comply with the radio act of the government. For the former, we used a small vacuum chamber to cover the GV and kept the dewar leak-tight even when the GV was opened (Figure 9 b⁷). The GV can be opened and closed repeatedly using a handle on the ground. The top part of the chamber was replaced with an RF transmissive window made of high-density polyethylene. For the latter, a radio-anechoic chamber made of Al with the radio absorber interior was placed on top of the chamber in the air (Figure 9 a). The S- or X-band antenna was placed inside (Figure 9 d) to emit power provided by a signal generator toward the microcalorimeter. The S-band antenna was made and characterized in-house and the X-band antenna was borrowed from the OMOTENASHI project²⁸ using a close frequency. A dipole antenna was placed 3 m away from the radio anechoic chamber to monitor the RF leakage using a spectral analyzer. As the RF injection path is only through the opened GV, the small radio-anechoic chamber suffices for the test purpose.

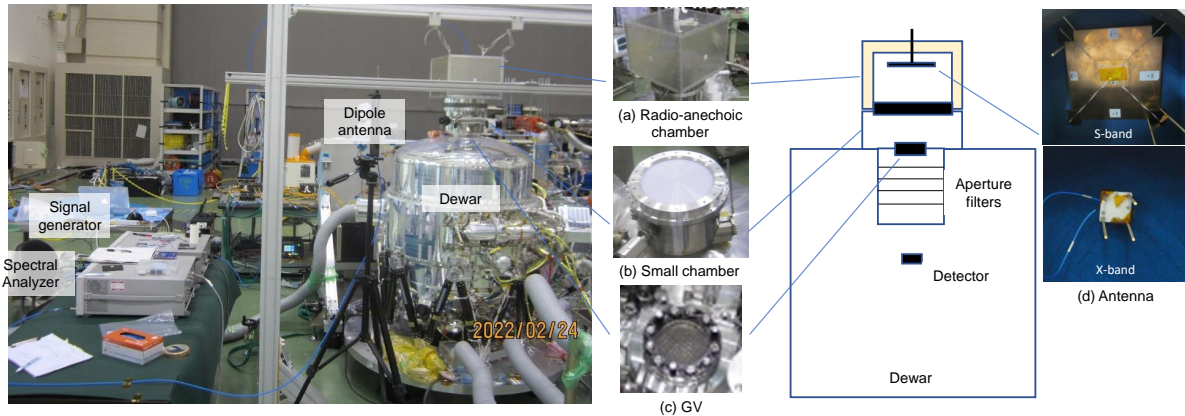


Fig 9: Setup for the RF EMI instrument-level test. (Left) photo of the setup. (Right) configuration and close-up views of some major apparatuses.

The injection level was increased from -120 dBm to 0 dBm by a 20 dB increment for the S and X-band in both the GV closed and open configurations. When the monitor was about to exceed the legal limit, the strongest injection was replaced with -10 dBm. The carrier frequency was amplitude-modulated at 73.5 Hz so that the modulated power is visible in the detector bandpass. At each injection, we obtained the $8k$ noise spectra of the microcalorimeter and measured the power at 73.5 Hz. Figure 10 shows the $8k$ noise spectra of some selected pixels in the strongest injection case of each configuration. No significant excess noise at the modulation frequency was observed in any of the measurements. The upper limit was $15\text{--}20$ nV/ $\sqrt{\text{Hz}}$, which is negligible for any degradation of the detector performance. No interference was detected on the anti-co signal either.

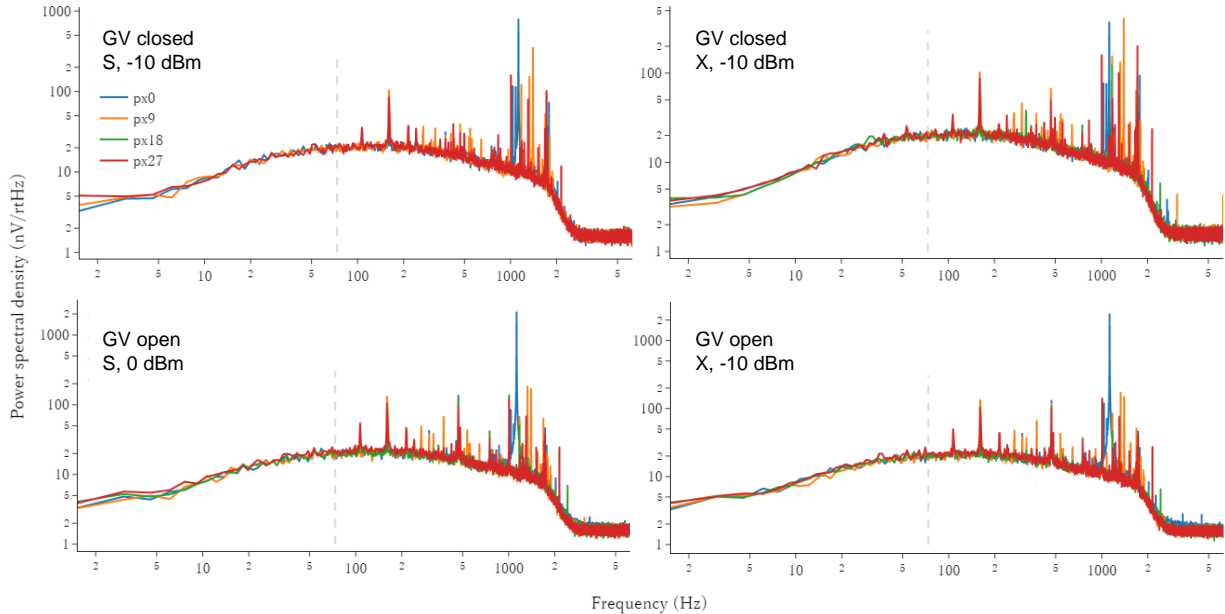


Fig 10: Results of the RF EMI instrument-level test. 8k noise spectrum of pixel 0, 9, 18, and 27 against the strongest RF injection. The dashed line shows 73.5 Hz.

4.3 Spacecraft-level test

We cannot open the GV in the spacecraft configuration on the ground, so no end-to-end assessment is possible when the spacecraft RF system is operating. We placed the X-band antenna, which was used as a transmitter in the instrument-level test (§ 4.3) and used it as a receiver in the spacecraft-level test, at a place close to the dewar entrance (Figure 11) and monitored the level of the field inside the spacecraft during the spacecraft-level tests. When the RF systems were operated in various modes for the air-link communication testing in June, 2022, the maximum measured level was about -80 dBm, which validates the assumed input level in the instrument-level test (§ 4.2) based on the simulation (§ 4.1).

4.4 Discussion

By combining the simulation and tests, we found that the microcalorimeter in *Resolve* was found immune to the RF input from the open hole in the top of the dewar when the GV is opened. The RF input of 1 mW, which corresponds to the maximum injection power at the instrument-level test (§ 4.2), is larger by many orders than the x-ray input from the same direction during observations of $\mathcal{O}(1$ fW) for a milli-Crab source. The microcalorimeter is protected against the input in electromagnetic forms of longer wavelengths than x-rays by the multiple layers of thin filters made of aluminized polyimide in the x-ray aperture.²⁹ For RF input, the Al in the filters of a 50–100 nm thickness reflects back most of the incoming power at its surface by the impedance mismatch with the vacuum, allowing only a small fraction (less than -50 dB) to penetrate. We speculate that multiple layers of such filters work effectively to reject RF noise input.

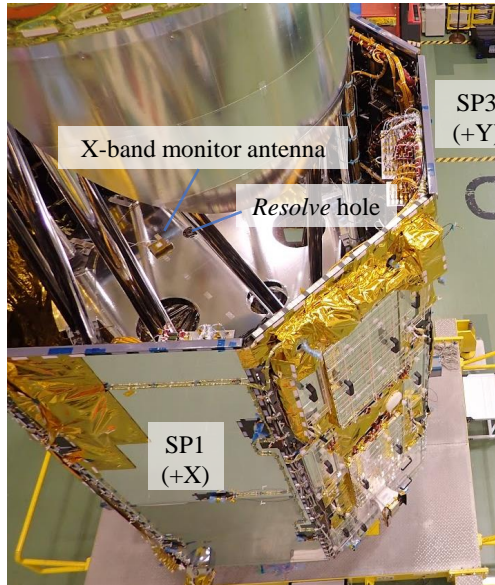


Fig 11: Setup for the RF EMI spacecraft-level test. An X-band antenna was installed on top of the lower plate close to the hole in the *Resolve* optical path. The photo was taken from the top of SP1 and SP2 in the downward-looking direction before the integration was completed.

5 Summary

We presented the results of the ground testing and simulation of the EMI to the x-ray microcalorimeter in the *Resolve* instrument onboard the XRISM. We discussed the magnetic EMI caused by the MTQs in the spacecraft attitude control system and the RF EMI caused by the spacecraft communication system. For the magnetic EMI, we observed a strong response in the microcalorimeter and anti-co time- and frequency-domain data. We speculated its coupling mechanisms based on the test and simulation results. There is no evidence that the resultant degradation is beyond the current allocation of noise budget. For the RF EMI, we injected RF signal up to 0/–10 dBm for the S/X-band but did not observe any response in the microcalorimeter and anti-co data in the instrument-level test. Because no end-to-end assessment is possible for the RF EMI on the ground, we conducted a full RF simulation using a detailed spacecraft CAD model and a single solver with Fugaku to complement the limitation. We found that the expected levels of the field diffracted from the spacecraft antennas are much smaller (–106/–63 dBm for S/X-band) than the level that *Resolve* was tested to be immune.

Acknowledgments

This work is made possible with significant contributions of all the XRISM *Resolve* team members, and the SHI and NEC engineers, which we greatly appreciate. Kenji Fukunabe, Yoshiaki Mitsutake, Atsushi Tomiki, Yutaro Sekimoto, Hayato Takakura at ISAS helped us to prepare for the instrument-level tests. This work used computational resources of the supercomputer Fugaku provided by RIKEN. This paper is a derivation of the SPIE proceeding.³⁰

References

- 1 J. A. Tauber *et al.*, “Planck pre-launch status: The Planck mission,” *antike und abendland* **520**, A1 (2010).

- 2 J. M. Lamarre *et al.*, “Planck pre-launch status: The HFI instrument, from specification to actual performance,” *antike und abendland* **520**, A9 (2010).
- 3 R. Gualtieri *et al.*, “SPIDER: CMB polarimetry from the edge of space,” *Journal of Low Temperature Physics* **193**, 1112–1121 (2018).
- 4 T. Takahashi *et al.*, “The ASTRO-H (hitomi) x-ray astronomy satellite,” in *Space Telescopes and Instrumentation 2016: Ultraviolet to Gamma Ray*, J.-W. A. den Herder, T. Takahashi, and M. Bautz, Eds., **9905**, 99050U, SPIE (2016).
- 5 R. L. Kelley *et al.*, “The Astro-H high resolution soft x-ray spectrometer,” in *Space Telescopes and Instrumentation 2016: Ultraviolet to Gamma Ray*, J.-W. A. den Herder, T. Takahashi, and M. Bautz, Eds., **9905**, 99050V (2016).
- 6 K. Mitsuda *et al.*, “Soft x-ray spectrometer (SXS): The high-resolution cryogenic spectrometer onboard ASTRO-H,” in *Space Telescopes and Instrumentation 2014: Ultraviolet to Gamma Ray*, T. Takahashi, J.-W. A. den Herder, and M. Bautz, Eds., **9144**, 91442A (2014).
- 7 Y. Ishisaki, R. L. Kelley, H. Awaki, *et al.*, “Status of resolve instrument onboard x-ray imaging and spectroscopy mission (XRISM),” in *Space Telescopes and Instrumentation 2022: Ultraviolet to Gamma Ray*, **12181**, 409–430, SPIE (2022).
- 8 M. S. Tashiro *et al.*, “Status of x-ray imaging and spectroscopy mission (XRISM),” in *Space Telescopes and Instrumentation 2020: Ultraviolet to Gamma Ray*, J.-W. A. den Herder, K. Nakazawa, and S. Nikzad, Eds., **11444**, 176, SPIE (2020).
- 9 M. E. Eckart, J. S. Adams, K. R. Boyce, *et al.*, “Ground calibration of the Astro-H (Hitomi) soft x-ray spectrometer,” in *Journal of Astronomical Telescopes, Instruments, and Systems*, T. Takahashi, J.-W. A. den Herder, and M. Bautz, Eds., **4**, 1, SPIE (2018).
- 10 F. S. Porter, K. R. Boyce, M. P. Chiao, *et al.*, “In-flight performance of the soft x-ray spectrometer detector system on Astro-H,” *Journal of Astronomical Telescopes, Instruments, and Systems* **4**, 1 (2018).
- 11 M. A. Leutenegger *et al.*, “In-flight verification of the calibration and performance of the ASTRO-H (Hitomi) Soft X-ray Spectrometer,” *Journal of Astronomical Telescopes, Instruments, and Systems* **4**, 021407 (2018).
- 12 C. A. Kilbourne *et al.*, “Design, implementation, and performance of the Astro-H SXS calorimeter array and anticoincidence detector,” *Journal of astronomical telescopes, instruments, and systems* **4**(1), 011214 (2018).
- 13 M. P. Chiao *et al.*, “System design and implementation of the detector assembly of the Astro-H soft x-ray spectrometer,” *Journal of Astronomical Telescopes, Instruments, and Systems* **4**(2), 1–16 (2018).
- 14 Y. Ishisaki *et al.*, “Resolve instrument on X-ray astronomy recovery mission (XARM),” *Journal of Low Temperature Physics* **193**, 991–995 (2018).
- 15 R. Fujimoto *et al.*, “Performance of the helium dewar and the cryocoolers of the Hitomi soft x-ray spectrometer,” *JATIS* **4**, 1 (2017).
- 16 S. Yoshida, “Cooling system for the soft X-ray spectrometer onboard the ASTRO-H,” *TEION KOGAKU (Journal of Cryogenics and Superconductivity Society of Japan)* **53**, 349–354 (2018).

- 17 P. J. Shirron, M. O. Kimball, B. L. James, *et al.*, “Design and on-orbit operation of the adiabatic demagnetization refrigerator on the Hitomi Soft X-ray Spectrometer instrument,” in *Space Telescopes and Instrumentation 2016: Ultraviolet to Gamma Ray*, J.-W. A. den Herder, T. Takahashi, and M. Bautz, Eds., **9905**, 99053O, International Society for Optics and Photonics (2016).
- 18 Y. Sato *et al.*, “Development of mechanical cryocoolers for the cooling system of the Soft X-ray spectrometer onboard Astro-H,” *Cryogenics* **52**, 158–164 (2012).
- 19 G. A. Sneiderman *et al.*, “Cryogen-free operation of the Soft X-ray Spectrometer instrument,” *JATIS* **4**, 1 (2018).
- 20 K. Kanao *et al.*, “Cryogen free cooling of ASTRO-H SXS helium dewar from 300 K to 4 K,” *Cryogenics* **88**, 143–146 (2017).
- 21 T. Midooka *et al.*, “X-ray transmission calibration of the gate valve for the x-ray astronomy satellite XRISM,” *Journal of Astronomical Telescopes, Instruments, and Systems* **7**(2), 028005 (2021).
- 22 T. Hasebe, R. Imamura, M. Tsujimoto, *et al.*, “Ground test results of the micro vibration interference for the x-ray microcalorimeter onboard XRISM,” in *Space Telescopes and Instrumentation 2022: Ultraviolet to Gamma Ray*, **12181**, 1527–1539, SPIE (2022).
- 23 R. Imamura, M. Tsujimoto, H. Awaki, *et al.*, “Results of accelerometer monitor in the ground testing of Resolve x-ray microcalorimeter instrument onboard XRISM,” in *X-Ray, Optical, and Infrared Detectors for Astronomy X*, **12191**, 763–770, SPIE (2022).
- 24 D. M. Sullivan, *Electromagnetic Simulation Using the FDTD Method*, John Wiley & Sons (2013).
- 25 K. Yee, “Numerical solution of initial boundary value problems involving Maxwell’s equations in isotropic media,” *IEEE Transactions on antennas and propagation* **14**(3), 302–307 (1966).
- 26 M. Sato *et al.*, “Co-design for a64fx manycore processor and” fugaku”, in *SC20: International Conference for High Performance Computing, Networking, Storage and Analysis*, 1–15, IEEE (2020).
- 27 J. Ahrens, B. Geveci, and C. Law, “ParaView: An End-User Tool for Large-Data Visualization,” in *Visualization Handbook*, C. D. Hansen and C. R. Johnson, Eds., 717–731, Butterworth-Heinemann, Burlington (2005).
- 28 T. Hashimoto *et al.*, “Nano semihard moon lander: OMOTENASHI,” *IEEE Aerospace and Electronic Systems Magazine* **34**(9), 20–30 (2019).
- 29 C. A. Kilbourne *et al.*, “Design, implementation, and performance of the Astro-H soft x-ray spectrometer aperture assembly and blocking filters,” *Journal of Astronomical Telescopes, Instruments, and Systems* **4**(1), 011215 (2018).
- 30 M. Kurihara, M. Tsujimoto, M. Eckart, *et al.*, “Ground test results of the electromagnetic interference in the x-ray microcalorimeter onboard XRISM,” in *Space Telescopes and Instrumentation 2022: Ultraviolet to Gamma Ray*, **12181**, 1445–1458, SPIE (2022).

Miki Kurihara is a graduate student of the University of Tokyo (astronomy major) working for XRISM at JAXA/ISAS. He received his BS in physics from Chiba University in 2021. He is a student member of SPIE.

List of Figures

- 1 Illustration of the spacecraft and the *Resolve* instrument. (Photo (c) is from Ishisaki et al.⁷)
- 2 Simulation models of (a) magnetic and (b) RF EMI seen from the SP7 in a slightly upward direction. The emission sources (a; three MTQs and b; two RF antennas) and the evaluation plane of the simulation (a; circular cross section perpendicular to the z axis including the feed-through and b; cross section perpendicular to the x axis including the detector center) are shown in red dashed-and-dotted curve or line.
- 3 Results of the magnetic simulation. The magnetic field strength $|\mathbf{B}|$ is given in the unit of μT on the plane perpendicular to the z axis at the height of the feed-through of the dewar harness leading to the ADRC/XBOX (Figure 2 a). The position of the detector and the feed-through is shown with the cross and the circle, respectively.
- 4 Setup for the magnetic EMI instrument-level test: (a) SP5 and (b) SP8 side of the dewar (Figure 3), and (c) drive electronics.
- 5 Results of the magnetic EMI instrument-level test: (a) Frequency-domain data of pixel 9 with varying detector bias (blue for nominal, violet for high, and orange for none) with a 30% PWM duty of the MTQ. The PWM frequency (127 Hz) and its second harmonics are shown with dashed lines. Data of nominal bias without MTQ operation (green) is shown for comparison. The 150 and 156 Hz lines are, respectively, the third harmonic of the commercial AC and a cryocooler drive.^{22,23} (b) Time-domain data of the drive voltage (blue) and response of the microcalorimeter for pixel 9 (orange), 27 (green), and the anti-co (red) during the 20% (solid) and 80% (dashed) duty drive. The anti-co signal is intrinsically opposite in polarity and shifted slightly in phase from that of the microcalorimeter. (c) Pixel dependence of the noise power at 127 Hz when the MTQ was operated with a 30% PWM duty using the 8k noise spectra. Pixel 12 yielded no noise spectra by being interrupted by constant x-ray illumination by the ^{55}Fe calibration source.
- 6 Results of the magnetic EMI spacecraft-level test: (a) Line power of px 9 at $127n$ Hz ($n = 1, 2, 3$) for the three MTQ units operated at $\pm 45\%$ duty ratio. The underlying continuum was subtracted. The error bars are estimated from the continuum levels of the frequency neighbors. The upper limit of 3σ is given in case of no detection. (b) Line power at 127 Hz for different duty ratio in the instrument- and spacecraft-level tests.
- 7 Comparison of the measurement and simulation: (a) Distance dependence of the 127 Hz power (pixels 9 and 27) and the simulated magnetic field strength $|\mathbf{B}|$ at the dewar center in the instrument-level test (§ 3.2) with the EM MTQ driven at a 30% duty. (b) Axis dependence of the 127 Hz power (pixels 9 and 27) and the simulated magnetic field strength $|\mathbf{B}|$ at the dewar center in the spacecraft-level test (§ 3.3) with the flight MTQs driven at a 45% duty.

- 8 Results of the RF simulation for the (a) S-band and (b) X-band antenna on SP7. The field strength $|\mathbf{E}|$ is given in the unit of V m^{-1} on the plane vertical to the x -axis including the detector (Figure 2 b). The interface is marked with the magenta cross. The horizontal structure from the antennas is an artifact of the simulation. Paraview²⁷ is used for visualization.
- 9 Setup for the RF EMI instrument-level test. (Left) photo of the setup. (Right) configuration and close-up views of some major apparatuses.
- 10 Results of the RF EMI instrument-level test. 8k noise spectrum of pixel 0, 9, 18, and 27 against the strongest RF injection. The dashed line shows 73.5 Hz.
- 11 Setup for the RF EMI spacecraft-level test. An X-band antenna was installed on top of the lower plate close to the hole in the *Resolve* optical path. The photo was taken from the top of SP1 and SP2 in the downward-looking direction before the integration was completed.